Kinematics of a balanced vane pump with circular tip vanes

Mattia Battarra[a,*], Alessandro Blum[b], Emiliano Mucchi[a]

[a]*University of Ferrara, Engineering Dept.*
Via G. Saragat, 1 - 44122
Ferrara, IT
[b]*ZF Friedrichshafen AG, Ostellato Plant*
Via M. Buonarroti, 2 - 44020
San Giovanni di Ostellato (FE), IT

Abstract

This paper analyzes the kinematics of the vane-cam ring mechanism in balanced vane pumps, by considering both vanes with centered and not-centered circular tip. The motion of the vane, the position of the contact point and the evolution of the pressure angle are analytically determined in reference to a generic cam ring profile. The results of the kinematic analysis are used to obtain the constraints defining the admissibility of the vane geometry, which is described in terms of tip radius, vane thickness and tip center eccentricity. A parametric study is performed to show the capabilities of the proposed formulation and the influence of the vane design parameters on its kinematics. The analysis demonstrates that the vane kinematic motion in balanced vane pumps is mainly controlled by the tip radius and the tip center eccentricity, as long as the cam ring profile is defined. The tip radius is mainly responsible for the shape of the vane motion, while the tip center eccentricity has a major influence on its timing. Furthermore the effect of the cam ring profile is evaluated by demonstrating that shape and extension of the rise and fall phases influence on the vane geometry admissibility.

Keywords: Vane pump, cam ring, pump kinematics, design constraint.

1. Introduction

Balanced vane pumps are widely adopted positive displacement machines, especially in the automotive field, where they are appreciated for their compactness, quietness and reliability. However, these results are usually achieved through complex and expensive
5　design processes involving large experimental campaigns and multi-disciplinary competences [1, 2], since many design parameters must concurrently satisfy requirements referring to wear resistance, fluid-dynamic performance and Noise, Vibration and Harshness (NVH) behavior.

In this scenario, the majority of the studies presented in the specialized literature
10　are focused on investigating various fluid-dynamic aspects by means of zero-dimensional

---

models [3, 4] and dedicated experimental campaigns [5]. In particular, Seet G. G. et al. in [6] introduced a computer model to evaluate the effect of silencing grooves on the delivery flow ripple and a similar approach was implemented by Watton J.J. et al. in [7] to evaluate the correct groove timing. Both studies are supported by measured data on efficiency and pressure ripple, in order to support the quality of the estimations. Similar studies have been proposed also by Nakamura K. et al. in [8] and by Jones B. et al in [9], with the purpose to enlighten the parameters producing the deepest impact on the model results. The approach at the basis of these studies coincides with the one adopted for the modeling of other positive displacement machines such as gear pumps [10, 11, 12], gerotor pumps [13] and axial piston pumps [14].

The modeling strategy described in these works has been also adopted to analyze other pump characteristics that can be put in correlation with its fluid-dynamic performance. Within this context, Hattori K. et al. in [15] adopted a zero-dimensional model to evaluate the delivery pressure ripple as the main source of emitted noise. A comparable approach has been also adopted by Cho M. R. et al. in [16], but in this context the predicted pressure distribution is used to estimate the loads applied to the vanes and consequently detect vane detachment phenomena. In both studies, the cam ring profile

2

is clearly described as one of the key design parameters for its direct influence on the vane motion and the pumping behavior of the machine. Similar considerations may be also derived from the work in [17] by Inaguma Y. and Nakamura K., in which the zero-dimensional fluid-dynamic approach is applied to a pump under test. In this context, the main focus is devoted on the assessment of the effects produced by leakage flow variations on the outlet pressure ripple.

As it may be observed from this brief literature review, the vane-cam ring mechanism, i.e. the coupling between the sliding vanes and the external ring of the pump, assumes a fundamental role in defining the pump behavior and its performance. The key character played by the vane-cam ring interaction was firstly investigated by Gellrich R. et al. in [18] with a mathematical model of the lubricated contacts that was tailored on the vane pump tribological system. The analysis was supported by a consistent experimental study reported in [19]. Later, the central role of the vane-cam ring mechanism in the wear phenomenon has been further underlined by Mucchi E. et al. in [20], where an extended experimental study has been conducted to evaluate the vane-cam ring interaction from a tribological point of view. The lubrication regime has been identified by means of pressure distribution measurements, as well as cam ring and vane surface measurements, with the final purpose of its evaluations in reference to different temperature values and pump materials. The influence of the vane-cam ring mechanism on the delivery pressure ripple has been also investigated with a theoretical approach. Giuffrida A. et Lanzafame R. in [21] described the cam ring profile as the main responsible for the definition of the kinematic pressure ripple generated by the vane pockets. In addition, the vane motion, which is also showed to be governed by this fundamental design parameter, resulted the main responsible for the characterization of the under vane kinematic pressure ripple. Giuffrida and Lanzafame proposed a complete procedure for estimating the theoretical pressure ripple starting from the definition of the cam ring geometry and the relaxed hypothesis of squared tip vanes.

Since the importance of controlling the vane motion and the vane-cam ring interaction is widely recognized in the specialized literature, it is the present authors' belief that a formalization of the kinematics of such a mechanism would deepen the understanding of its behavior and facilitate the development of further investigations on these machines. The kinematic analysis is the definition of the rigid body motion of the mechanism in absence of dynamic effects, hence, it defines the displacing action of positive displacement pumps. Based on these considerations, the purpose of the present work is to provide a general formalization of the kinematics of the vane-cam ring mechanism in case of circular tip vanes, by developing the methodology on a realistic schematic of the pump. The analysis is carried out for both centered and not-centered tip vanes, with the intent to involve the main influencing parameters. The definition of the vane motion, the position of the contact point, as well as the analytic determination of the kinematic pressure angle, are included within the outcome of the analysis. As a major result, the kinematic properties of the mechanism are linked to the geometrical constraints defining the vane shape to obtain the admissibility domain for the vane geometry, i.e. the set of values ensuring that the vane-cam ring mechanism is inherently compliant. This last step of the analysis provides design boundary conditions for the geometrical definition of the vanes. In addition, the proposed method may find its application in tools for performance prediction since it allows to *i)* estimate displacement, velocity, acceleration and jerk of the vanes, which are directly related to the pump dynamic behavior, *ii)* calculate the pres-

3

sure angle determining the components of the variable contact force applied to the vane and the cam ring, *iii)* calculate the vane radial velocity, which coincides with the volume derivative of the under-vane pockets, giving a relevant contribution to the definition of the delivery flow rate and pressure ripples. The results of the overall kinematic analysis are numerically evaluated by means of a parametric study applied to dimensionless linkages, in order to provide general results referring to the interactions between the vane kinematics and the main design parameters.

The following Section describes the kinematics of the vane-cam ring mechanics, starting with the definition of vane motion through the closure equation, which is then adopted to obtain the analytic formulation of the pressure angle and the admissibility interval for the vane tip radius. Section 3 presents the results of the parametric study carried out to clarify the influence of the cam ring profile on the vane motion, explaining also how the proposed formulae can be used as design guidelines for the vane geometry definition. Finally, Section 4 is devoted to concluding remarks.

2. Kinematic analysis of the vane-cam ring mechanism

The present Section is focused on the kinematic analysis of the vane-cam ring mechanism, with the purpose to define the vane motion in reference to the position of the contact point, the pressure angle and the admissibility of the vane geometry. The analysis is carried out for both not-centered and centered circular tip vanes, where the latter is considered as a special case of the first one. Figure 1.a represents a cross-sectional view of a balanced vane pump: the machine is constituted by an internal rotor that forces the vanes to rotate from the inlet side to the delivery one. The internal profile of the cam ring, which is the main responsible for the pumping action of the machine, governs the radial motion of each vane. Starting from $\gamma = 0$, the radius of the cam ring increases progressively, after a brief dwell interval, until it reaches a maximum value: during this phase the volume of the pocket bounded by two consecutive vanes expands and fills itself with oil from the inlet port. Such a pocket is then displaced to the delivery port through the precompression zone and finally released to the outlet port. In order to provide a perfect balancing of the rotor, this layout is repeated twice per revolution. It is therefore clear that the cam ring profile requires a careful design, since its shape defines both the radial movement of the vanes and the pumping action of the entire machine. In this context, the cam ring profile can be represented by a Rise-Fall-Dwell (R-F-D) law (see Figure 1.b), which is mainly defined on the basis of fluid-dynamic considerations and the required pump displacement.

2.1. Vane kinematic motion

The generic vane-cam ring mechanism, in case of not-centered circular tip vanes, can be represented by the equivalent mechanical linkage system described in Fig. 2, where link #1 represents the pump rotor, link #2 is the vane and link #3 constitutes the cam ring. The case of centered circular tip vanes can be described by the same linkage by assuming segment $\overline{CQ}$ equal to zero. The basic application of the Grübler's criterion can demonstrate that the proposed mechanism has a single degree of freedom. The closure equation describing the position of contact point P with respect to the angular position
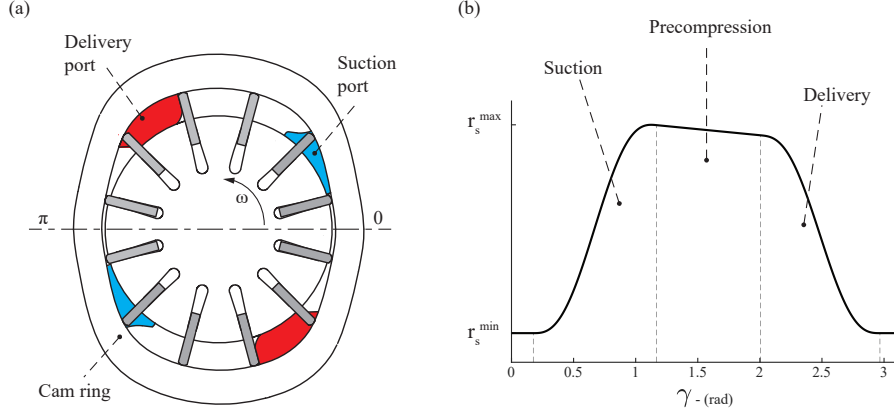
4

Figure 1: Generic representation of a balanced vane pump (a) and cam ring profile on a cartesian plane (b). Parameters r_s^{max} and r_s^{min} are the cam ring maximum and minimum radii, respectively.

of the vane θ, therefore becomes:

$$(r_r + h(\theta)) e^{i\theta} + d e^{i\left(\theta + \frac{\pi}{2}\right)} + r_v e^{i(\theta + \beta)} = r_s(\gamma) e^{i\gamma} \tag{1}$$

where r_r is the radius of the internal rotor, h is the displacement of point Q with respect to the rotor and r_v represents its radius. Term d, namely the vane tip eccentricity, defines the position of the center of the circle describing the vane tip with respect to the longitudinal axis of the vane, which coincides with segment OQ in Fig. 2. It is worth clarifying that term d must be kept together with its sign, which is assumed as positive when it produces a counterclockwise rotation of segment OC with respect to OQ. Radius r_s and angle γ describe the position of the contact point P in terms of polar coordinates of the cam ring (see also Fig. 1.b), while angle β is the pressure angle between the vane tip and the cam ring. It is worth noticing that usually the geometrical features of the pump, such as vane and rotor dimensions as well as the cam ring profile, are defined *a priori* and therefore Eq. 1 can be adopted to determine the actual vane displacement $h(\theta)$. As it emerges from the pump description in the first paragraph, the vane-cam ring linkage may be considered as a cam-follower mechanism where the cam is fixed and the follower rotates around it. The antithetical relationship between these two mechanisms is made clear also by the design philosophy typically followed for their definition: in the cam-follower mechanism, the R-F-D law is assigned to the follower and the designer must determine the profile of the cam that guarantees the required follower motion. On the contrary, in the vane-cam ring mechanism the cam ring profile is assigned in order to perform a predefined pumping action and the vane displacement becomes a dependent variable.

On the basis of these considerations, Eq. 1 is constituted by two unknowns, which are vane displacement vector $\bar{h}$ defined by polar coordinates (h, θ) and pressure angle β. By referring to Fig. 3, the pressure angle may be linked to the vane angular position by using the scalar relationship:

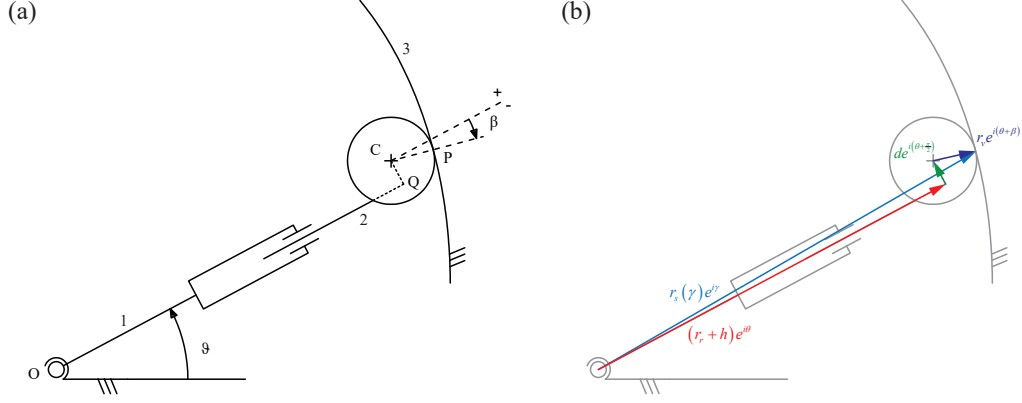$$\theta + \beta = \gamma - \psi \tag{2}$$

5

Figure 2: <mark>Equivalent mechanical linkage representing the vane-cam ring mechanism (a) and schematic representation of the closure equation (b). As reported, angle β is taken positive when counterclockwise.</mark>

<mark>where the positive sign for each angle is defined by a counterclockwise rotation. In addition, it is worth noticing that angle ψ is the angle between the tangent to the cam ring profile at the contact point and the perpendicular line with respect to radius $r_s\left(\gamma\right)$. As a matter of fact, such a term can be calculated by computing the derivative of the cam ring radius with respect to angle γ:</mark>

$$\psi = \tan^{-1}\left[\frac{1}{r_s^{min}}\left.\frac{\delta r_s}{\delta\gamma}\right|_P\right] \tag{3}$$

<mark>therefore, given the cam ring geometry, angle ψ is known.</mark> The nonlinear equation system given by Eqs. 1 and 2 can be effectively used to determine the kinematic displacement of the vane in polar coordinates (h,θ) and pressure angle β, once the remaining geometrical parameters are fully defined:

$$\begin{cases} \left(r_r + h\left(\theta\right)\right)e^{i\theta} + de^{i\left(\theta+\frac{\pi}{2}\right)} + r_v e^{i(\theta+\beta)} = r_s\left(\gamma\right)e^{i\gamma} \\ \theta + \beta = \gamma - \psi \end{cases} \tag{4}$$

It is worth underlining that, by assuming $d = 0$, the obtained equation system can be adopted to analyze the case of vanes with centered circular tip. Under this hypothesis, Eq. 4 reduces to:

$$\begin{cases} \left(r_r + h\left(\theta\right)\right)e^{i\theta} + r_v e^{i(\theta+\beta)} = r_s\left(\gamma\right)e^{i\gamma} \\ \theta + \beta = \gamma - \psi \end{cases} \tag{5}$$

2.2. Pressure angle

Despite Eq. 4 provides a complete description of the kinematics of the linkage, it is worth deepening the analysis in order to enlighten the mutual relationship between pressure angle β and the geometrical characteristics of the system. <mark>As a matter of fact, the pressure angle represents a key reference indicator since it controls the component of the contact force that is normal to the vane axis and it defines the position of the</mark>
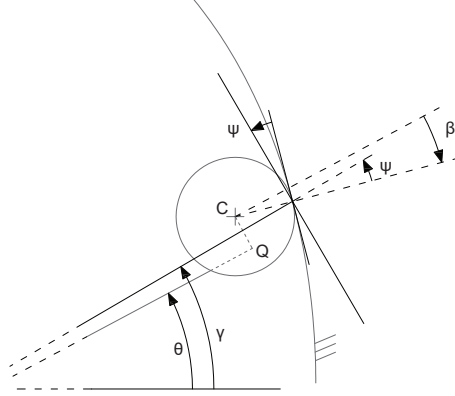
6

Figure 3: Focus on the relationship between pressure angle β and vane angula position θ.

which is defined by the angular sector constituting the tip of the vane (see Fig. 4). With this purpose, by using Eq. 2 in order to define γ with respect to θ, Eq. 1 may be rewritten as:

$$(r_r + h(\theta)) e^{i\theta} + de^{i\left(\theta + \frac{\pi}{2}\right)} + r_v e^{i(\theta + \beta)} = r_s(\gamma) e^{i(\theta + \beta + \psi)} \tag{6}$$

Since Eq. 6 must be valid for each angular position of the vane, it may be reduced to:

$$r_r + h(\theta) + de^{i\frac{\pi}{2}} + r_v e^{i\beta} = r_s(\gamma) e^{i(\beta + \psi)} \tag{7}$$

which actually expresses the displacement of the vane with respect to a reference system that is centered in O and rotates together with the vane itself. By focusing the attention on the imaginary part of Eq. 7

$$d + r_v \sin\beta = r_s \sin(\psi + \beta) \tag{8}$$

after some manipulation, the following relationship is obtained:

$$d + (r_v - r_s \cos\psi) \sin\beta = r_s \sin\psi \cos\beta \tag{9}$$

Therefore, by considering the case $d = 0$, the closed-form expression for the pressure angle simply becomes:

$$\beta = \tan^{-1}\left[\frac{r_s \sin\psi}{r_v - r_s \cos\psi}\right] \tag{10}$$

in the open interval $-\frac{\pi}{2} < \beta < \frac{\pi}{2}$. It is worth noticing that Eq. 10 states that, for centered circular tip vanes, pressure angle β strictly depends on the cam ring profile, its first angular derivative and the vane tip radius. In particular, pressure angle β tends to increase both with the increment of the vane tip radius and the increment of the first derivative of the cam ring profile. On the basis of these considerations, Eq. 10 can

be used to determine the pressure angle course along a complete revolution, without the necessity to estimate the vane kinematic motion and before the geometry of the vane-cam ring mechanism is fully defined.

In the more general scenario of $d \neq 0$, a closed-form expression for the pressure angle can still be obtained, even if its achievement is less straightforward. With the help of the substitution:

$$t = \tan\left(\frac{\beta}{2}\right) \tag{11}$$

then:

$$\sin\beta = \frac{2t}{1+t^2} \tag{12}$$

$$\cos\beta = \frac{1-t^2}{1+t^2} \tag{13}$$

Equations 12 and 13 may now be substituted into Eq. 9 obtaining:

$$d + (r_v - r_s\cos\psi)\frac{2t}{1+t^2} = r_s\sin\psi\frac{1-t^2}{1+t^2} \tag{14}$$

Since the denominator in Eq. 14 is strictly positive, the problem is reduced to the solution of the following quadratic equation:

$$(d + r_s\sin\psi)\,t^2 + 2\,(r_v - r_s\cos\psi)\,t + (d - r_s\sin\psi) = 0 \tag{15}$$

By solving Eq. 15 and applying the substitution in Eq. 11, the following expression for pressure angle β is obtained:

$$\beta = 2\tan^{-1}\left[\frac{r_s\cos\psi - r_v \pm \sqrt{r_s^2 + r_v^2 - 2r_v r_s\cos\psi - d^2}}{d + r_s\sin\psi}\right] \tag{16}$$

The right choice of the sign before the squared term depends on which side of the cam ring profile the contact will take place. Since in a vane-cam ring mechanism the contact always takes place on the inner side of the cam ring profile, the squared term must be negative and therefore the correct expression becomes:

$$\beta = 2\tan^{-1}\left[\frac{r_s\cos\psi - r_v - \sqrt{r_s^2 + r_v^2 - 2r_v r_s\cos\psi - d^2}}{d + r_s\sin\psi}\right] \tag{17}$$

It is worth underlining that the radicand in Eq. 17 is always positive by construction and therefore no further conditions are required in order to avoid imaginary roots. In order to clarify this aspect, it is possible to focus the attention on segment $\overline{OC}$ in Fig. 2. By applying the cosine formula with respect to angle $O\hat{P}C$:

$$\overline{OC}^2 = r_s^2 + r_v^2 - 2r_v r_s\cos\psi \tag{18}$$

the following equality can be recognized:

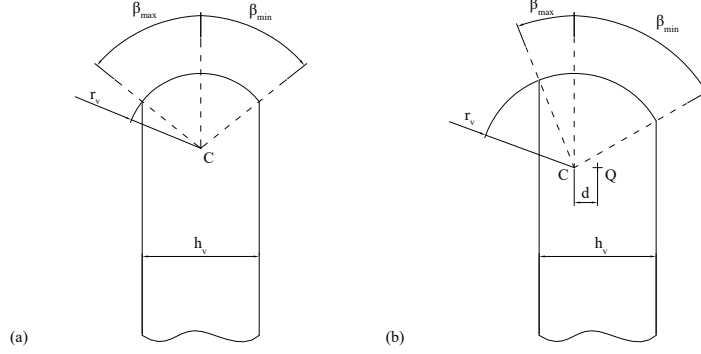$$r_r + h = \sqrt{r_s^2 + r_v^2 - 2r_v r_s\cos\psi - d^2} \tag{19}$$

8

Figure 4: Design parameters for centered tip vanes (a) and not-centered tip vanes (b).

which demonstrates that the radicand is always strictly positive since term $r_r + h$ is strictly positive by construction. In addition, Eq. 19 may represent a useful alternative to Eq. 1 for estimating the vane motion amplitude h without the necessity to solve the nonlinear system reported in Eq. 4. However, the complete definition of the vane motion given by the two parameters (θ, h) still requires to solve also Eq. 2, which is possible once β has been already calculated. By using the equality in Eq. 19, the expression for pressure angle β may be finally rewritten as:

$$\beta = 2\tan^{-1}\left[\frac{r_s \cos\psi - r_v - (r_r + h)}{d + r_s \sin\psi}\right] \qquad (20)$$

which demonstrates that, in case of not-centered circular tip vanes, pressure angle β depends on the cam ring profile, its first angular derivative and the vane tip radius as well as the vane tip eccentricity, but its determination is subordinate to the calculation of the vane motion amplitude h.

2.3. Admissibility of the vane geometry

The proposed analysis has provided useful tools to calculate the vane motion and the pressure angle, both obtained in reference to the exact position of the contact point. Moreover, it has enlightened their relationship with some design parameters of the vane-cam ring mechanism itself. However, by focusing the attention on the vane geometry, it is possible to obtain further indications related to its admissibility in reference to the cam ring profile. As shown in Fig. 4, the vane tip profile, which is constituted by a circular arc bounded by the lateral vane flanks, provides a practical limit on the maximum and minimum values that the pressure angle is allowed to assume, i.e. β_{max} and β_{min} respectively:

$$\beta_{min} \leq \beta \leq \beta_{max} \qquad (21)$$

In the special case $d = 0$ (Fig. 4.a), the vane shape is symmetrical with respect to its longitudinal axis through point C. In this scenario, pressure angle limits β_{max} and β_{min}

9

can be determined as:

$$\beta_{max} = -\beta_{min} = \tan^{-1}\left[\frac{h_v}{\sqrt{4r_v^2 - h_v^2}}\right] \tag{22}$$

where h_v represents the vane thickness. Hence, by substituting Eqs. 10 and 22 into Eq. 21, it is possible to translate the angular constraint into a design constraint referred to the tip radius:

$$\left|\tan^{-1}\left[\frac{r_s \sin\psi}{r_v - r_s \cos\psi}\right]\right| \leq \tan^{-1}\left[\frac{h_v}{\sqrt{4r_v^2 - h_v^2}}\right] \tag{23}$$

Since the inverse tangent is a monotonic function, the proposed inequality reduces to:

$$\left[\frac{r_s \sin\psi}{r_v - r_s \cos\psi}\right]^2 \leq \left[\frac{h_v{}^2}{4r_v^2 - h_v^2}\right] \tag{24}$$

which can be solved with respect to tip radius r_v. In this context, the standard form becomes:

$$r_v^2\left[h_v^2 - 4r_s^2 \sin^2\psi\right] - r_v\left[2h_v^2 r_s \cos\psi\right] + h_v^2 r_s^2 \geq 0 \tag{25}$$

The roots of the related polynomial can be therefore obtained straightforwardly:

$$r_{v_{lim}}^{1,2} = \frac{h_v^2 r_s \cos\psi \pm h_v^2 r_s \sin^2\psi \sqrt{4r_s^2 - h_v^2}}{h_v^2 - 4r_s^2 \sin^2\psi} \tag{26}$$

Consequently, the solution of the inequality expressed by Eq. 25 is given by the interval:

$$\left(-\infty, \min\left(r_{v_{lim}}^{1,2}\right)\right] \wedge \left[\max\left(r_{v_{lim}}^{1,2}\right), +\infty\right) \tag{27}$$

Similarly to the considerations related to Eq. 16, it is possible to notice that the higher interval, i.e. $\left[\max\left(r_{v_{lim}}^{1,2}\right), +\infty\right)$, can be neglected since it refers to the case where the contact takes place on the external side of the cam ring profile. In practice, root $\min\left(r_{v_{lim}}^{1,2}\right)$ represents the maximum value that the tip radius is allowed to assume. In addition, by focusing on Fig. 4, it must be taken into account that the vane geometry provides also the following constraint:

$$r_v \geq \frac{h_v}{2} \tag{28}$$

which practically represents a limit on the minimum allowable value for the vane tip. Thus, from Eqs. 27 and 28, tip radius r_v must stand within $\frac{h_v}{2}$ and $\min\left(r_{v_{lim}}^{1,2}\right)$, where the latter may assume two different expressions depending on the sign of the first derivative of the cam ring profile. In particular, tip radius r_v must observe the following relationship:

$$\frac{h_v}{2} \leq r_v \leq \min\left(r_{v_{\lim}}^{1,2}\right) = \begin{cases} \frac{h_v^2 r_s \cos\psi - h_v r_s \sin\psi \sqrt{4r_s^2 - h_v^2}}{h_v^2 - 4r_s^2 \sin^2\psi} & for \quad \psi \geq 0 \\ \frac{h_v^2 r_s \cos\psi + h_v r_s \sin\psi \sqrt{4r_s^2 - h_v^2}}{h_v^2 - 4r_s^2 \sin^2\psi} & for \quad \psi < 0 \end{cases} \tag{29}$$

Equation 29 mathematically defines the conditions to be respected to ensure the admissibility of the vane geometry. In practice, if Eq. 29 is satisfied, it is guaranteed that the vane-cam ring mechanism is inherently compliant, meaning that the mechanism can

It is worth noticing that, while the lower boundary in Eq. 29 is fixed by the vane thickness, the upper boundary depends on both the vane thickness and the cam ring profile, meaning that such a limit assumes a different value for each point of the cam ring. By taking into account that the cam ring profile may be described by a R-F-D law, during the dwell phase, angle ψ coincides with zero and the upper boundary becomes $\min\left(r_{v_{\lim}}^{1,2}\right) = r_s$. On the contrary, during both the rise and fall phases, the upper boundary changes point by point depending on the mathematical law adopted to describe such phases. Hence, given the vane thickness and the cam ring profile, the overall upper boundary is defined by the minimum value assumed by term $\min\left(r_{v_{\lim}}^{1,2}\right)$ along a complete revolution. However, from these considerations it follows that, for any cam ring profile, radius r_v will never be allowed to overcome the upper limit constituted by r_s^{min}.

In the more general scenario with $d \neq 0$, the vane tip profile becomes asymmetric (see Fig, 4.b) and therefore maximum and minimum allowable values for pressure angle β become:

$$\beta_{\max} = \tan^{-1}\left[\frac{h_v - 2d}{\sqrt{4r_v^2 - (h_v - 2d)^2}}\right] \tag{30}$$

$$\beta_{\min} = -\tan^{-1}\left[\frac{h_v + 2d}{\sqrt{4r_v^2 - (h_v + 2d)^2}}\right] \tag{31}$$

Hence, the constraint condition given by Eq. 21 may be rewritten in the following form:

$$\begin{cases} \frac{2\tan(\beta/2)}{1-\tan^2(\beta/2)} \leq \frac{h_v - 2d}{\sqrt{4r_v^2 - (h_v - 2d)^2}} & for \quad \beta \geq 0 \\ \frac{-2\tan(\beta/2)}{1-\tan^2(\beta/2)} > \frac{h_v + 2d}{\sqrt{4r_v^2 - (h_v + 2d)^2}} & for \quad \beta < 0 \end{cases} \tag{32}$$

where term $\tan(\beta)$ has been defined with respect to $\tan(\beta/2)$, since no analytical expression for $\tan(\beta)$ are available in the case $d \neq 0$. In order to obtain a design constraint similar to Eq. 27, it would be now necessary to substitute Eq. 17 into both terms of Eq. 32 and then solve it with respect to radius r_v. However, in the present case, the purpose to obtain an analytical solution appears to be less suitable, since the presence of multiple quadratic terms leads to inequalities with polynomials of order much higher than two. For this reason, the most convenient approach is represented by the numerical one, where the roots of the polynomial in Eq. 32 can be searched within the interval defined by Eq. 29. The result of this analysis, in analogy with the case $d = 0$, will produce the upper boundary of the interval defining the admissible values for radius r_v. On the other hand, based on the same considerations made for the case $d = 0$, the lower boundary of such an interval is defined by the practical constraint:

$$r_v \geq \frac{h_v}{2} + |d| \tag{33}$$

The proposed procedure will be further clarified in the following Section, where the analysis is applied to a realistic pump geometry and the influence of the different design parameters is evaluated.

3. Parametric study

The present Section analyzes the results that are achievable with the equations provided in Section 2. In particular, Subsection 3.1 focuses the attention on the relationship existing between cam ring profile and vane geometry in the centered tip scenario, while Subsection 3.2 extends them to the not-centered tip case. The analysis is performed on a given cam ring profile, which is used as reference datum to define the admissible vane geometry and the influence of the vane design parameters on the vane motion itself. Later, in Subsection 3.3 the study concentrates on determining how the cam ring profile affects the admissibility of the vane geometry and its kinematics. In this context, the adoption of a precompression zone as well as different mathematical laws describing rise and fall sections are evaluated in detail, in order to provide a complete overview of the kinematic characteristics of the vane-cam ring mechanism.

With the purpose to provide general results and avoid the necessity to refer to a specific pump geometry, all the geometrical parameters are expressed with respect to minimum cam ring radius r_s^{min} on the basis of the Buckingham's Theorem [22]. By defining pump displacement per facewidth unit as:

$$V = 2\pi \left(r_s^{max2} - r_s^{min2} \right) \tag{34}$$

the proposed dimensional reduction allows us to define the specific pump displacement as:

$$\hat{V} = 2\pi \left(\hat{e}^2 - 1 \right) \tag{35}$$

where term $\hat{e}$ is the ratio between r_s^{max} and r_s^{min}. With the proposed dimensional reduction, given term $\hat{e}$, it is possible to refer to a family of pump characterized by the same specific displacement. By adopting this dimensional reduction for all the pump geometrical parameters, it is possible to state that two pumps with different size but same specific geometrical parameters will be kinematically equivalent. On the basis of this statement, all the parameters in the following study are considered in their specific form, identified by symbol $\hat{\cdot}$.

3.1. Centered tip vane layout

The present Subsection enlightens the deep connection between cam ring profile and vane geometry with respect to the definition of the vane-cam ring kinematics. The analysis is focused on the zero tip eccentricity layout. In order to fulfill this purpose, the cam ring profile shown in Fig. 5 is taken as reference, where both rise and fall phase are obtained with a 5th order polynomial law. Parameter $\hat{e}$ has been chosen equal to $\sqrt{1 + 1/2\pi}$ in order to obtain $\hat{V} = 1$. For the sake of clarity, the precompression rate has been set to zero and its influence is analyzed in Subsection 3.3, where the effect of different values of the specific pump displacement are also evaluated.

Since the cam ring profile is defined, the first set of achievable information refers to the admissibility of the vane geometry. In this context, Eq. 26 can be adopted to determine the evolution of the upper limit value for vane tip radius $\hat{r}_v$ along the cam ring profile in reference to the vane thickness, in the case $\hat{d} = 0$. Within this framework, the course of radius $r_{v_{lim}}$ for a complete period of the cam ring and five values of $\hat{h}_v$ is reported in Fig. 6. As previously discussed by describing Eq. 26, during the dwell phases radii $\hat{r}_{v_{lim}}^{1,2}$
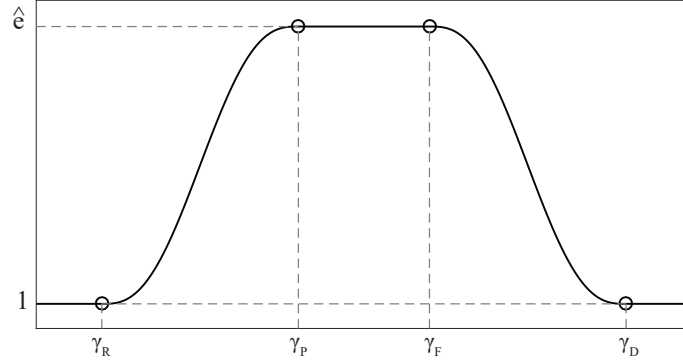
12

Figure 5: Reference cam ring profile where γ_R and γ_P respectively represent the first and last angular instants of the rising phase, γ_F is the initial angular instant of the falling phase and γ_D indicates the starting of the dwell phase.

Table 1: Design parameter values related to the reference cam ring profile in Fig. 5.

$\hat{e}$	$\sqrt{1 + 1/2\pi}$
γ_R	$\pi/10$
γ_P	$2\pi/5$
γ_F	$3\pi/5$
γ_D	$9\pi/10$

coincide with cam ring radius $\hat{r}_s$, while they bifurcate during both rise and fall phases. The curves that stand above $\hat{r}_s$ are referred to the case where the contact takes place on the external side of the cam ring profile and they are therefore neglected in Fig. 6. In this scenario, the most relevant aspect is the behavior of the minimum value assumed by $\hat{r}_{v_{lim}}$,

320   which tends to increase as the vane thickness increases. This trend is underlined further by Eq. 29 that describes the admissibility interval for vane tip radius $\hat{r}_v$ with respect to vane thickness $\hat{h}_v$, as shown in Fig. 7. As it is expected, while $\hat{r}_v^{min}$ is increasing linearly, the upper limit represented by $\hat{r}_v^{max}$ follows a nonlinear law that suddenly tends to one as $\hat{h}_v$ increases. In particular, it is worth noticing that, independently from the cam ring

325   shape, the admissible domain is always bounded by two intersections between $\hat{r}_v^{max}$ and $\hat{r}_v^{min}$ occurring for $\left(\hat{h}_v, \hat{r}_v\right) = (0,0)$ and $\left(\hat{h}_v, \hat{r}_v\right) = (2,1)$. The first one constitutes the trivial solution of Eq. 29, while the second one is a practical limit imposed by the cam ring profile itself: when $\hat{h}_v = 2$ the vane thickness and the minimum cam ring diameter coincide, constraining the vane tip radius $\hat{r}_v$ to be equal to $\hat{r}_s^{min}$.

330   Once the admissible values for $\hat{r}_v$ are determined, it is possible to evaluate how the vane tip radius affects the kinematic motion of the vane. Figure 8.(a) shows the variation of the vane displacement with respect to the cam ring profile for four different values of $\hat{r}_v$, which have been chosen in order to span all the admissible range for $\hat{h}_v = 0.1$. As it is also underlined by the zoom in Fig. 8.(b), as the vane tip radius increases, the vane

335   displacement tends to deviate from the cam ring profile during both rise and fall phases and such a phenomenon becomes more and more intense as the vane tip radius approaches
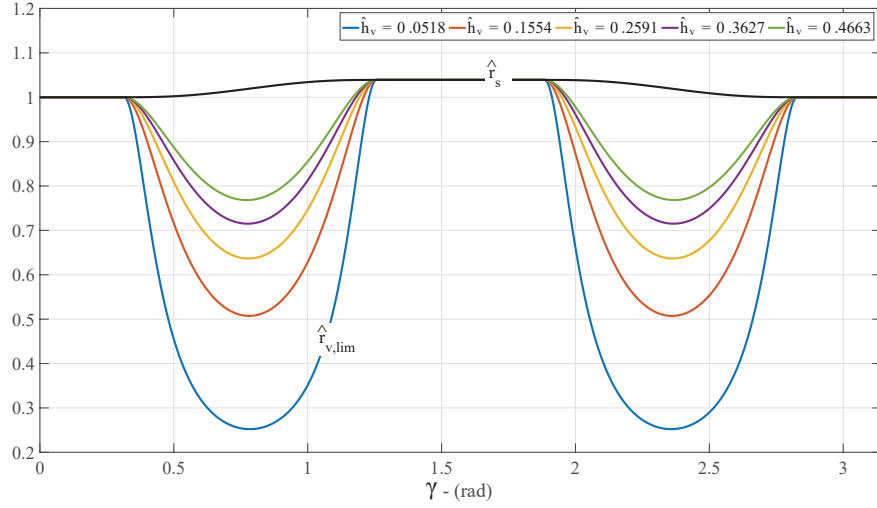
13

Figure 6: Evolution of upper boundary $\hat{r}_{v_{lim}}$ for a complete period of the cam ring and five values of $\hat{h}_v$.
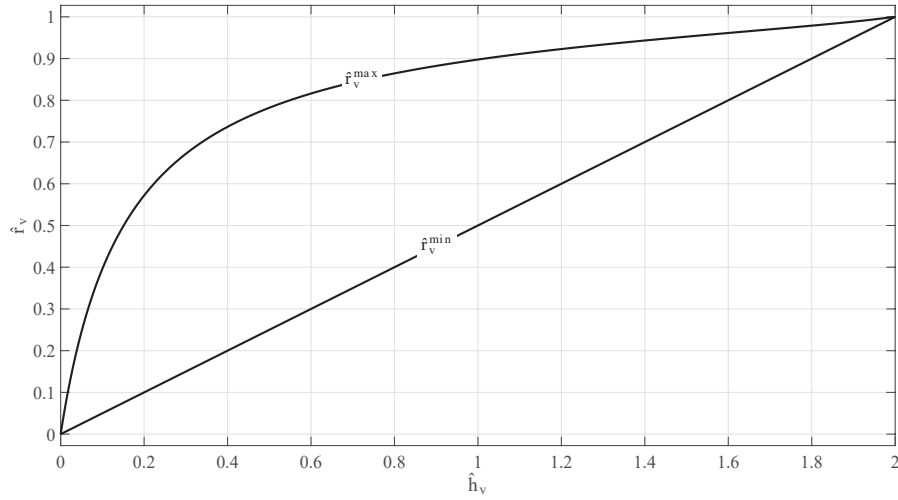

Figure 7: Admissibility interval for vane tip radius $\hat{r}_v$ with respect to vane thickness $\hat{h}_v$ in the case $\hat{d} = 0$.

the upper boundary of its admissible range. This aspect becomes even more evident by focusing the attention on velocity, acceleration and jerk associated to the vane motion, which are depicted in Fig. 9. While the $\hat{r}_v = 0.05$ case seems to reproduce the derivatives of the fifth order polynomial law describing the rise and fall phases approximately well, the $\hat{r}_v = 0.2809$ case shows an appreciable deviation from the expected shape and this behavior is particularly enhanced for the $\hat{r}_v = 0.3964$ condition. In this context, it is worth noticing that the variation of $\hat{r}_v$ influences the shape of the motion, but the timing
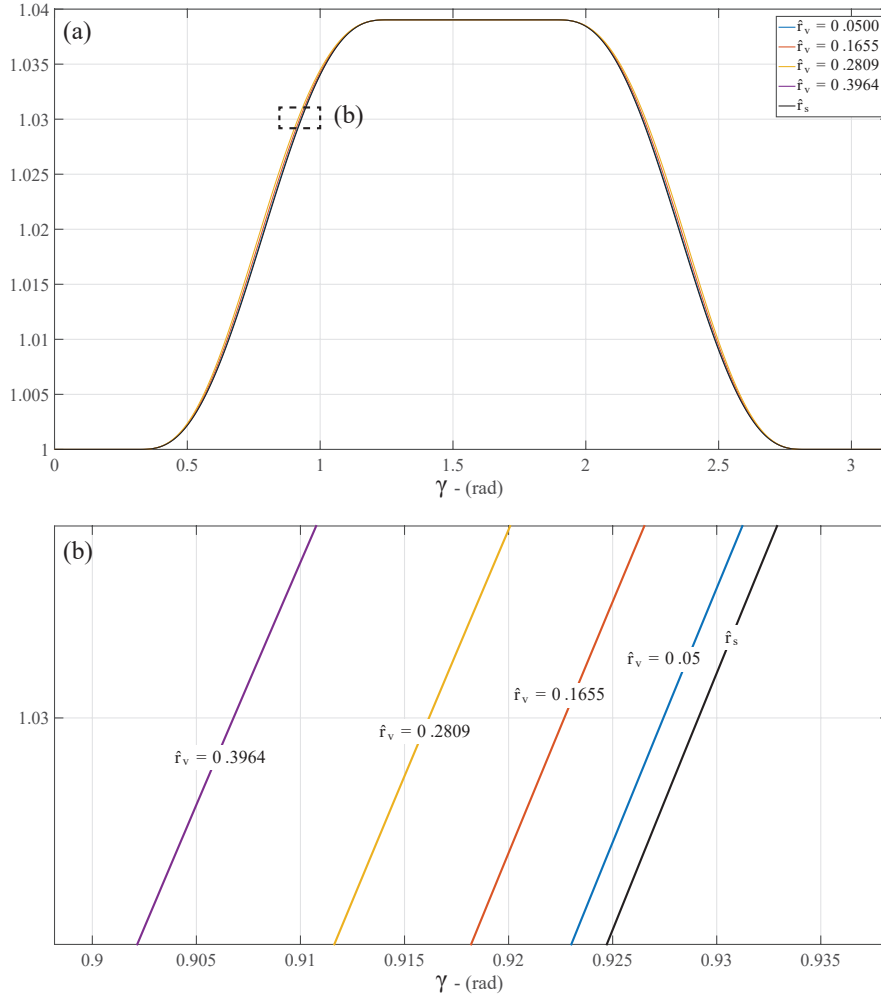
14

Figure 8: Comparison between the cam ring profile and the vane displacement for different values of the specific vane tip radius in the case $\hat{d} = 0$ (a) and detailed view of the deviation (b).

imposed by the cam ring profile is not distorted. The detected behavior differs from the results that are obtained by calculating the vane motion on the basis of the relaxed hypothesis of flat tip geometry, in which the vane thickness influences the timing of the vane motion while its shape remains unaltered [21].

Based on the purpose to provide a complete overview of the vane-cam ring kinematic behavior, the proposed analysis may be used also to evaluate pressure angle β of the contact force between the cam ring profile and the vane tip in the hypothesis of absence of friction. Figure 10 shows the obtained results for the four $\hat{r}_v$ values defined in the previous paragraph. As it can be appreciated, by rising the specific vane tip radius, the maximum and minimum values of β are slightly increased in their absolute value as well.
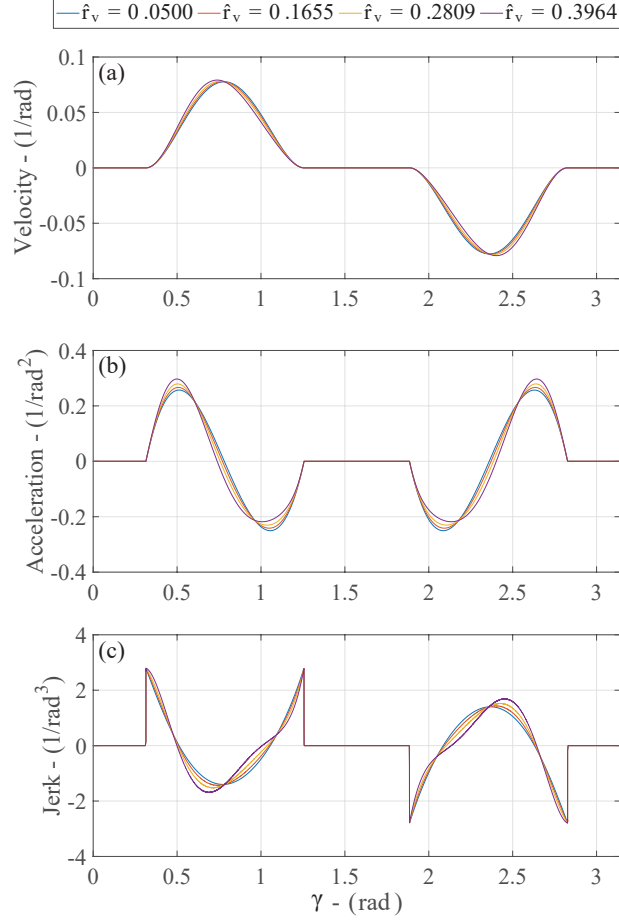
15

Figure 9: Vane kinematic characteristics in terms of velocity (a), acceleration (b) and jerk (c) for different values of the vane tip radius in the case $\hat{d} = 0$.

The observed behavior helps to understand the phenomenon that produces the upper boundary of the admissible range for the vane tip radius: starting from an admissible value of $\hat{r}_v$, as this parameter is rised, the maximum and minimum values reached by β slowly increases while the limits β_{max} and β_{min} defined in Eq. 22 decrease progressively (in terms of absolute values) until the inequality in Eq. 21 is no longer satisfied.

3.2. Not-centered tip vane layout

The study described in Subsection 3.1 has been carried out with the purpose to explain the relationship between vane thickness and tip radius and how the latter influences the motion of the vane in the hypothesis of zero tip eccentricity. In order to evaluate the effects produced by this last parameter, the analysis is now repeated for the more general scenario characterized by not-centered tip vanes (see Fig. 4). The study is performed
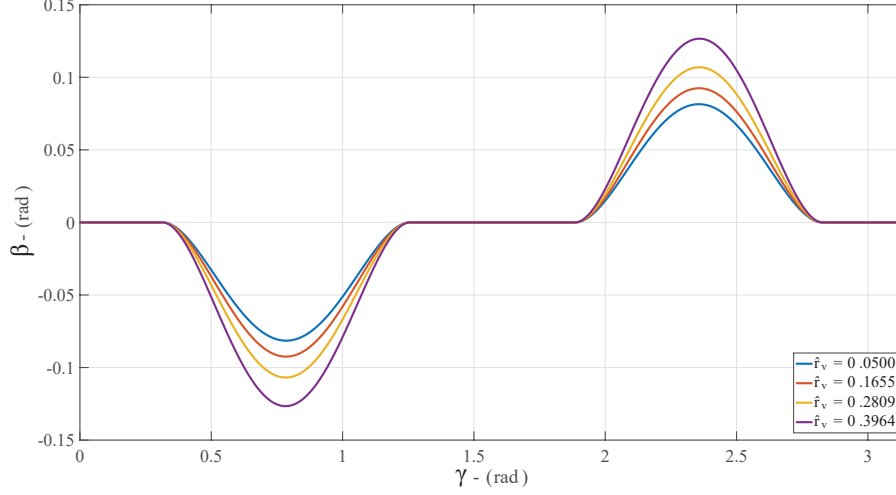
16

Figure 10: Evolution of pressure angle β along a complete period of the cam ring profile for different values of the vane tip radius in the case $\hat{d} = 0$.

==by considering the same cam ring profile defined in Subsection== 3.1. In this context, by solving Eq. 32 in conjunction with Eq. 33, the tri-dimensional surface in Fig. 11 representing the boundaries of the admissible domain for the combination of vane tip radius $\hat{r}_v$, vane thickness $\hat{h}_v$ and vane tip eccentricity $\hat{d}$ can be computed. However, due to the complex shape of the obtained geometry, the result may be better analyzed by extrapolating the isolines with respect to the available bi-dimensional planes. Figure 12, in particular, reports the isolines calculated with respect to the $\hat{d}\hat{r}_v - plane$: for each vane thickness value the admissible domain is bounded by a quadrilateral polygon that tends to expand itself and then collapse into a single point as $\hat{h}_v$ moves from zero to two. On the other hand, it is worth to noting that the center of the tip circle is always forced to fall within the vane thickness, since the vane tip eccentricity is well confined within the $\left| \frac{\widehat{h}_v}{2} \right|$ limit. Another interesting point of view is provided by Fig. 13, depicting the isolines obtained on the $\hat{h}_v\hat{r}_v - plane$ with respect to different values of the vane tip eccentricity. Obviously, the curve referring to the $\hat{d} = 0$ condition coincides with the result reported in Fig. 7. In this case, it may be observed that as $\hat{d}$ is varied from the centered layout, the admissibility range is reduced consistently due to the simultaneous effects of reducing the extension of the upper boundary and shifting up the lower one. The described behavior has also a major consequence on the practical design of vane layouts with $\widehat{r}_v = \frac{\widehat{h}_v}{2}$ and $\widehat{d} = 0$. This particular vane geometry is located on the lowest boundary defined in Fig. 13 and a small amount of eccentricity caused by a low quality production process would result in a not admissible combination of the parameters $\left(\hat{h}_v, \hat{r}_v, \hat{d} \right)$.

The definition of the available combinations for the triple $\left(\hat{h}_v, \hat{r}_v, \hat{d} \right)$ allows us to evaluate the influence of the vane tip eccentricity on the kinematic motion of the vane
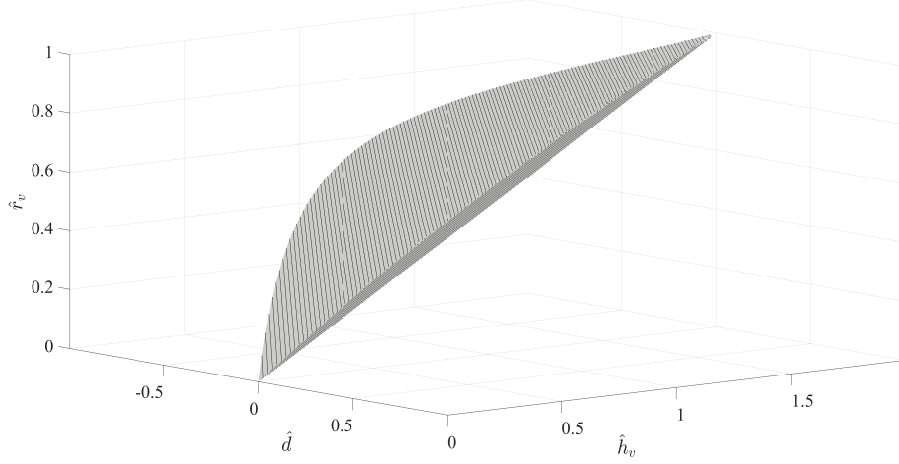
17

Figure 11: Surface defining the boundaries of the admissible domain for the combination of vane tip radius $\hat{r}_v$, vane thickness $\hat{h}_v$ and vane tip eccentricity $\hat{d}$.
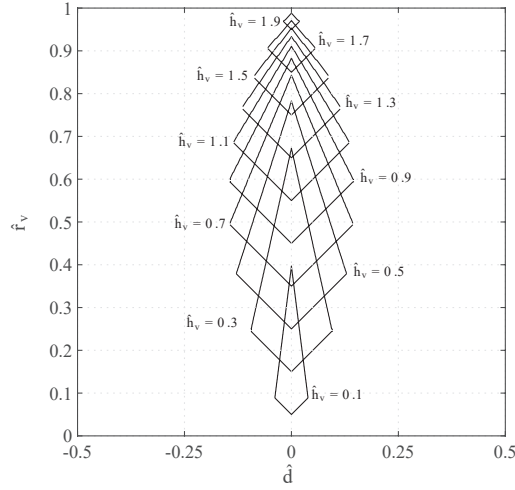

Figure 12: Isolines obtained by projecting the boundaries of the admissible domain on the $\hat{d}\hat{r}_v - plane$.

itself. In this framework, the vane displacement is compared with respect to cam ring profile $\hat{r}_s$ both in the case of positive eccentricity (Fig. 14) and negative eccentricity (Fig. 15). By considering a generic vane with $\hat{h}_v = 0.3$ and $\hat{r}_v = 0.88$, the former compares the case $\hat{d} = 0$ with the case $\hat{d} = -0.038$, which represent the limit value for $\hat{d} > 0$ according to Fig. 12. Similarly, Fig. 15 reports the comparison between the case $\hat{d} = 0$ with the case $\hat{d} = 0.038$ for the same combination of $\hat{h}_v$ and $\hat{r}_v$. As it can be noted, negative values of $\hat{d}$ produce two main effects: the first outcome is a delay in the timing of the
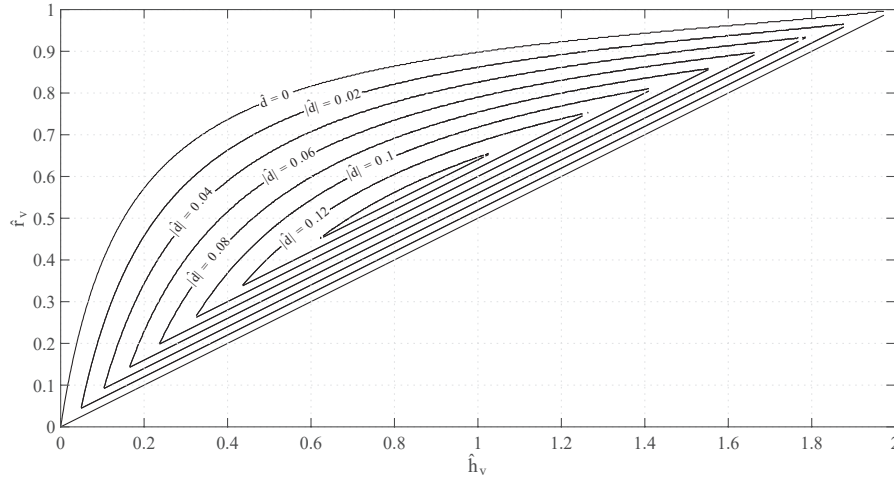
18

Figure 13: Isolines obtained by projecting the boundaries of the admissible domain on the $\hat{h}_v\hat{r}_v - plane$.
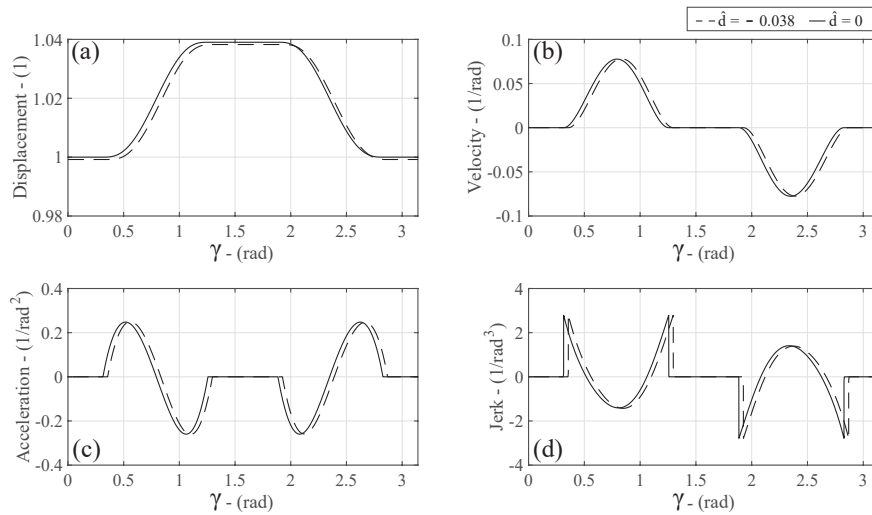

Figure 14: Effect of the negative tip eccentricity on the vane kinematic motion; results refer to a vane geometry with $\hat{h}_v = 0.3$ and $\hat{r}_v = 0.88$.

R-F-D law which tends to increase itself linearly with the eccentricity, while the second effect is a downward shift of the R-F-D law that becomes appreciable during both dwell phases (Fig. 14.a). This latter effect is obviously detected also in the case of positive values of d (Fig. 15.a), since positive and negative eccentricities are analogous layouts with respect to the dwell phase. On the other hand, the $d > 0$ condition causes an opposite consequence on the timing of the vane motion, since both rise and fall phases are advanced with respect to cam ring profile.
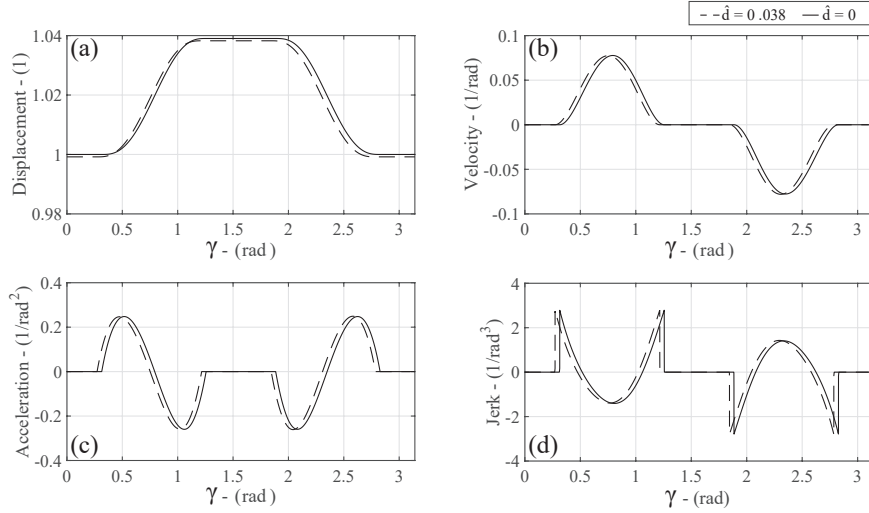
19

Figure 15: Effect of the positive tip eccentricity on the vane kinematic motion; results refer to a vane geometry with $\hat{h}_v = 0.3$ and $\hat{r}_v = 0.88$.

The influence on the timing of the vane motion is further enlightened by focusing the attention on velocity (Fig. 14.b), acceleration (Fig. 14.c) and jerk (Fig. 14.d) related to the vane displacement profiles defined in the previous paragraph. Moreover, the results referring to the second and third derivatives demonstrate that the adoption of a not-zero eccentricity layout produces a negligible effect on the shape of the vane displacement. As a matter of fact, concentrating on the charts in Fig. 14, it is possible to note a certain variation of the maximum and minimum values reached by velocity, acceleration and jerk for the three vane geometries, however, the magnitude of such a variation is extremely slight. The described behavior is observed also for positive values of the tip eccentricity, as clarified by Fig. 15 from b to d.

The proposed analysis demonstrates that the vane kinematic motion in balanced vane pumps is mainly controlled by the tip radius and the tip center eccentricity, as long as the cam ring profile is defined. The tip radius is mainly responsible for the shape of the vane motion, while the tip center eccentricity has a major influence on its timing. In addition, these two design parameters are linked to each other through the vane thickness that does not have a direct influence on the vane motion, but it defines the width of the admissible region in which the couple $(\hat{r}_v, \hat{d})$ can be chosen.

3.3. Cam ring profile influence

The previous Subsections have been used to explain how, given the cam ring profile, the mathematical laws obtained in Section 2 may be used to determine the admissible values for the main vane design parameters and how they affect the vane kinematic characteristics. In the present Subsection, on the contrary, the attention is concentrated on the cam ring profile and the way it influences the admissible vane geometry and its motion.
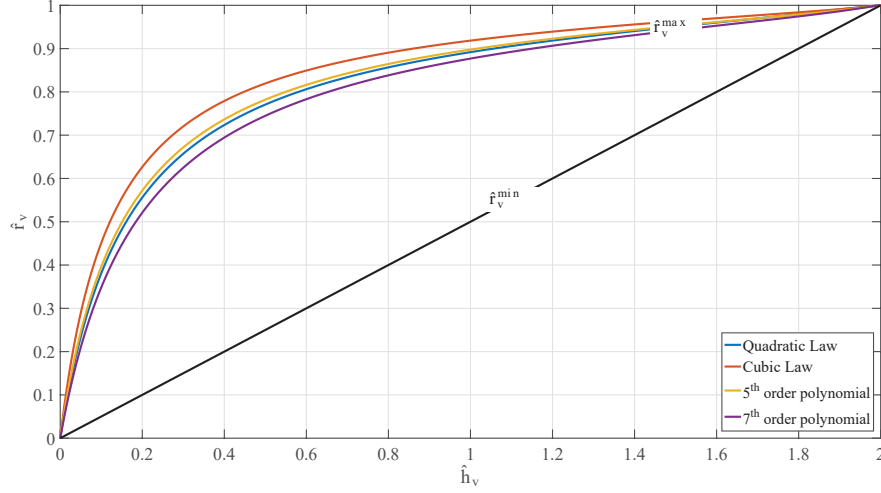
Figure 16: Admissibility interval for the couple $\left(\hat{h}_v, \hat{r}_v\right)$ related to different mathematical laws defining rise and fall phases of the cam ring profile, in the case $\hat{d} = 0$.

In this framework, the study is firstly focused on the mathematical laws defining rise and fall phases of the RFD law. As already demonstrated by Fig. 6, both rise and fall phases are responsible for defining the maximum allowable tip radius given the vane thickness and the tip eccentricity, since during the dwell phases, the maximum tip

430 radius coincides with the cam ring radius. Once the central role played by rise and fall sections is clarified, the aim is now to point out how the profile of rise and fall phases affect the available range of the vane geometry. With this purpose, Fig. 16 reports the admissibility intervals for the combination of $\hat{r}_v$ and $\hat{h}_v$ in the case $\hat{d} = 0$ related to four cam ring profiles, which share the same design parameters defined in Tab. 1 although

435 characterized by different mathematical laws performing the rise and fall phases. As it can be observed, moving from the most gradual law, i.e. the cubic one, to the sharpest one, i.e. the 7th order polynomial, the maximum allowable tip radius is reduced progressively. On the other hand, the lower boundary constituted by $\hat{r}_v^{min}$ remains unchanged, since it is exclusively defined by vane parameters $\hat{h}_v$ and $\hat{d}$. The same would apply in the

440 case where the cam ring profile utilizes two different laws to perform the rise and fall phases: the sharpest one would define the admissibility region since it represents the most restrictive condition.

A similar trend is detected also in the case where, given a fixed mathematical law, the angular extension of the rise (and/or fall) phase is gradually reduced. An example of

445 this behavior is depicted in Fig. 17, in which $\hat{r}_v^{max}$ is calculated with respect to the cam ring profile adopted in Subsection 3.1, that is modified by progressively anticipating the inception of the upper dwell phase. The explanation of this trend has to be detected in Eq. 29, which states that the maximum allowable tip radius depends on both the cam ring profile and its first derivative. Hence, as the rise and fall phases are made sharper,

450 limit value $\hat{r}_v^{max}$ decreases accordingly.

This latter analysis can be further deepened by including the tip eccentricity as a
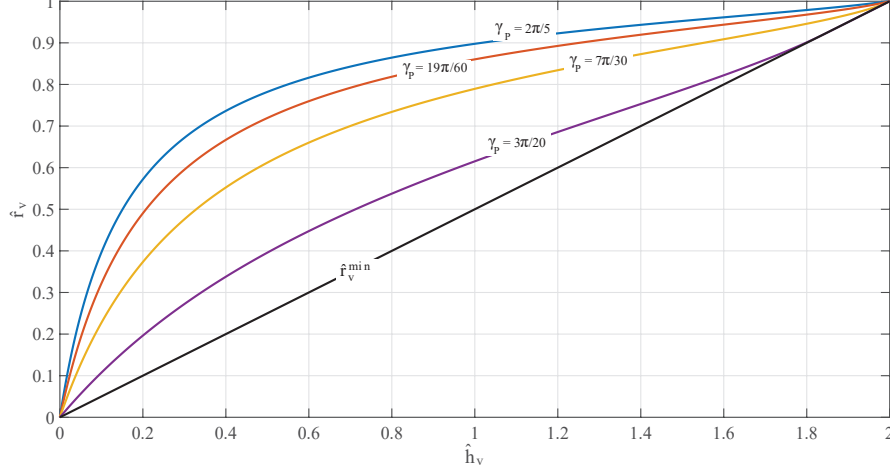
21

Figure 17: Variation of upper boundary limit $\hat{r}_v^{max}$ for different rise phase extensions, in the case $\hat{d} = 0$.

third variable. Within this framework, Fig. 18.a depicts the isolines of the vane geometry admissible domain on the $\hat{d}\hat{r}_v - plane$ related to the cam ring profile with $\gamma_P = 7\pi/30$. As described in the previous paragraph, this cam ring profile has an asymmetric shape since, the angular sector pertaining the rise phase is considerably shorter than the one pertaining the fall phase. As shown in Fig. 18.a, the geometrical asymmetry of the cam ring profile produces an asymmetric vane geometry admissible domain, which is bent towards positive values of the vane eccentricity. The described behavior may be better recognized by focusing the attention on the locus of the maximum allowable tip radius, i.e. the set of points constituting the upper vertices of the quadrilaterals in Fig. 18.a. Such points are not located along the $\hat{d} = 0$ axis as in the case of symmetric cam ring profile (as shown in Fig. 12), but they lay on a curved line that stays within the positive quarter of the $\hat{d}\hat{r}_v - plane$. The phenomenon is observed also in Fig. 18.b and 18.c, depicting the isolines of the same vane geometry admissible domain on the $\hat{h}_v\hat{r}_v - plane$.

A practical explanation for the described behavior may be obtained by analyzing the variation of β along a complete course. The pressure angle approaches negative values during the rise phase and positive one during the fall phase. Since in the analyzed cam ring the sharpest motion is performed on the rise phase, angle β reaches higher values (in magnitude) during the rise phase rather than during the fall phase. Therefore, by considering that the $\hat{d} > 0$ layout guarantees $|\beta_{\min}| > \beta_{\max}$, the positive eccentricity allows the mechanism to perform the motion with higher values of the tip radius in comparison to the negative eccentricity layout. As a matter of fact, the tip eccentricity may be considered as a tuning parameter in presence of cam ring profiles with a sharp rise (or fall) phase. In this framework, the adoption of a limited amount of tip eccentricity would provide the chance to adopt vane geometries with greater tip radius.

The last parameter which is now investigated is the adoption of a precompression zone. As reported also in [7, 16, 21], the upper dwell interval in balanced vane pumps
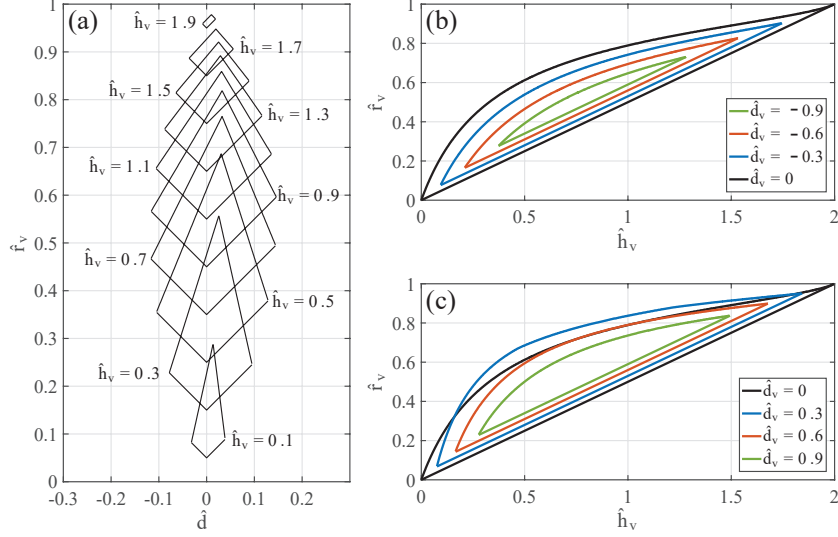
Figure 18: Vane geometry admissible domain for a cam ring profile with 5th order polynomial laws, $\hat{e} = \sqrt{1 + 1/2\pi}$ and $\gamma_R = \pi/10$, $\gamma_P = 7\pi/30$, $\gamma_F = 3\pi/5$ and $\gamma_D = 9\pi/10$. The domain is reported with respect to the $\hat{d}\hat{r}_v - plane$ in (a) and with respect to the $\hat{r}_v\hat{h}_v - plane$ in (b) and (c).

may be replaced by a slight precompression zone constituted by a linearly decreasing profile inserted between rise and fall phase. This design solution is typically adopted
480 to reduce the risk of discharging air bubbles into the delivery side and, concurrently, to produce a limited increase of the oil pressure within the displaced pocket. The magnitude of the precompression zone is defined by the precompression ratio ξ, which is defined as:

$$\xi = \frac{\hat{r}_s(\gamma_P) - \hat{r}_s(\gamma_F)}{\gamma_P - \gamma_F} \tag{36}$$

In order to evaluate the influence of this feature, the cam ring adopted in Subsection 3.1 is taken as reference benchmark and compared with three similar layouts that differs
485 from the reference one for the presence of a precompression zone with a progressively increasing precompression ratio, from $\xi = 0.1$ to $\xi = 0.3$. Figure 19 reports the described cam ring profiles.

With the purpose to clarify the effect produced by this common design solution, attention can be firstly focused on Fig. 20 showing the evolution of pressure angle β
490 along a complete course for the four cam ring profiles, in the case $\hat{d} = 0$ and $\hat{r}_v = 0.1655$. As expected, within the precompression zone, pressure angle β is steadily higher than zero, due to the linear profile of the cam ring. A more interesting aspect is the behavior of the pressure angle during rise and fall phases: since the former is made sharper while the latter is made duller, β is also made asymmetric. In particular, it shows a progressive
495 decrease of the minimum value reached during the rise phase despite its variation along the fall phase tends to be slightly flattened towards zero. It is worth clarifying that the choice of the tip radius value is based exclusively on the necessity to guarantee the admissibility of the vane geometry and the adoption of other values would not change
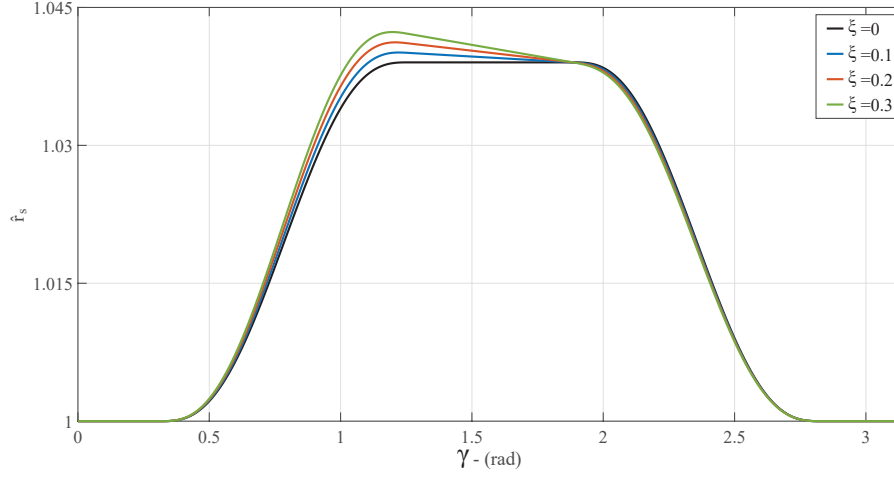
23

Figure 19: Cam ring profiles obtained with different values of precompression ratio ξ.
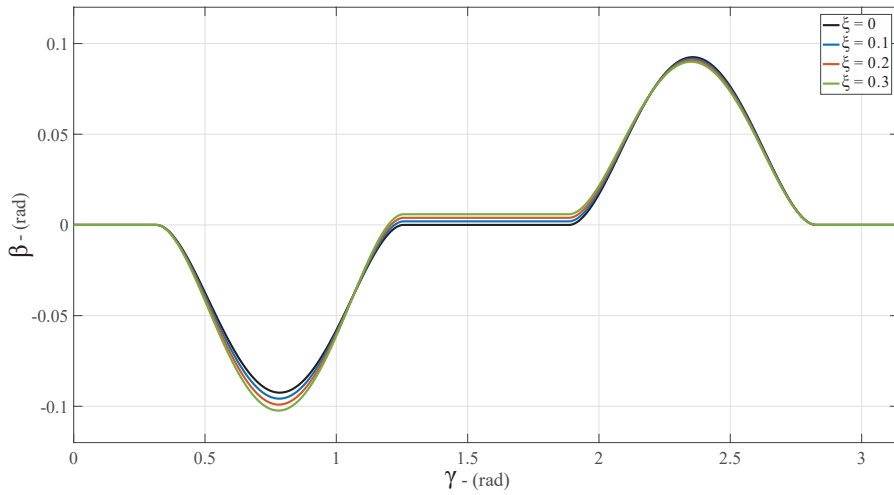

Figure 20: Pressure angle β along a complete cam ring period, related to the four precompression layout in Fig. 19.

the detected behavior.

From a practical perspective, since the effect on β is limited, the adoption of a pre-compression zone in the case $\hat{d} = 0$ does not produce a consistent effect on the vane kinematics and its geometry admissibility. On the other hand, by considering that this design choice affects the asymmetry of the vane motion, it is worth focusing the attention on its influence regarding the admissible domain related to not-centered tip vanes. Within this context, Fig. 21 reports the isolines on the $\hat{h}_v \hat{r}_v - plane$ referring to the
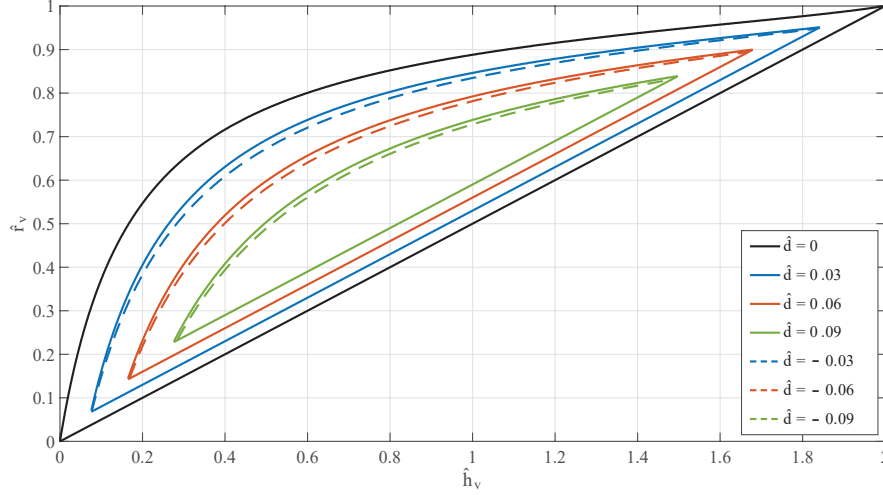
24

Figure 21: Isolines on $\hat{h}_v\hat{r}_v - plane$ obtained for the cam ring profile with $\xi = 0.3$ in Fig. 19.

vane geometry admissible domain calculated with respect to case $\xi = 0.3$. As previously observed by evaluating different rise phase extensions, the asymmetry of the vane motion is translated into an asymmetry of the admissible domain, however, in this case the locus of the maximum allowable tip radius does not bend but it remains located on the $\hat{d} = 0$ axis. On behalf of this result, it appears to be clear that this design solution does not interfere with the global behavior of the vane kinematics and the choice to neglect it in the previous analyses does not compromise the generality of the results.

4. Concluding remarks

The present work describes the kinematics of the vane-cam ring mechanism in balanced vane pumps, by taking into account the adoption of centered and not-centered tip vanes. The analysis is performed analytically, with the purpose to define the vane kinematic motion in reference to the main geometrical parameters of the vane, which are constituted by tip radius, vane thickness and tip eccentricity. The proposed methodology is able to localize the contact point in reference to the angular position of the vane, describe the vane displacement and compute the pressure angle between cam ring and vane tip. In addition, the kinematic laws are coupled with the vane practical constraints in order to analytically determine the admissibility of the vane geometry. Dedicated formulae have been derived for both centered and not-centered tip vanes.

In order to deepen the understanding of the vane geometry and its kinematic motion, a parametric study has been performed by considering both cam ring profile and vane geometry in their non-dimensional form, which is obtained with respect to the minimum value of the cam ring radius. As a first step, the vane geometry allowable domain is calculated and later both vane motion and pressure angle are evaluated with respect to a number of vane design layouts. The results clarify that the vane kinematic motion in balanced vane pumps is mainly controlled by the tip radius and the tip center eccentricity,

25

as long as the cam ring profile is defined. The tip radius is mainly responsible for the shape of the vane motion, while the tip center eccentricity has a major influence on its timing. In addition, these two design parameters are linked to each other through the vane thickness that does not have a direct influence on the vane motion, but it defines the width of the admissible region in which the couple $\left(\hat{r}_v, \hat{d}\right)$ can be chosen.

The last part of the parametric study is devoted to detect the influence of the cam ring shape on the vane kinematics. Within this framework, the most common mathematical laws adopted to perform rise and fall phases are taken into account, as well as different angular extensions and various precompression layouts. The analysis demonstrates that the size of the vane admissible domain tends to be decreased by the sharpness of the rise and fall phases. Moreover, the potential asymmetry of the vane motion imposed by the cam ring profile translates itself into an asymmetry of the admissible domain. A similar phenomenon is slightly produced also by the adoption of precompression schemes.

References

[1] J. Ivantysyn, M. Ivantysynova, Hydrostatic pumps and motors: principles, design, performance, modelling, analysis, control and testing, first engl Edition, Tech Books International, New Delhi, India, 2003.

[2] M. Rundo, N. Nervegna, Lubrication pumps for internal combustion engines: A review, International Journal of Fluid Power 16 (2) (2015) 59–74. `doi:10.1080/14399776.2015.1050935`.

[3] A. Bianchini, G. Ferrara, L. Ferrari, F. Paltrinieri, F. Tosetti, M. Milani, Design and Optimization of a Variable Displacement Vane Pump for High Performance IC Engine Lubrication: Part 1 - Experimental Analysis of the Circumferential Pressure Distribution with Dynamic Pressure Sensors, in: SAE World Congress & Exhibition, 2009, pp. 11–18. `doi:10.4271/2009-01-1045`.

[4] G. Cantore, F. Paltrinieri, F. Tosetti, M. Milani, Lumped Parameters Numerical Simulation of a Variable Displacement Vane Pump for High Speed ICE Lubrication, in: SAE Technical Paper, no. 724, 2008, p. 11. `doi:10.4271/2008-01-2445`.

[5] E. Mucchi, G. Cremonini, S. Delvecchio, G. Dalpiaz, On the pressure ripple measurement in variable displacement vane pumps, Journal of Fluids Engineering 135 (2013) 091103.

[6] G. G. Seet, J. E. Penny, K. Foster, Applications of a computer model in the design and development of a quiet vane pump, Proceedings of the Institution of Mechanical Engineers, Part B: Journal of Engineering Manufacture 199 (4) (1985) 247–253. `doi:10.1243/PIME_PROC_1985_199_076_02`.

[7] J. J Watton, K. L. Watkins-Franklin, The Transient Pressure Characteristic of a Positive Displacement Vane Pump, Proceedings of the Institution of Mechanical Engineers, Part A: Journal of Power and Energy 204 (4) (1990) 269–275. `doi:10.1243/PIME_PROC_1990_204_036_02`.

[8] K. Nakamura, A. Hibi, H. Yanada, Y. Hattori, Pressure Ripples of a Balanced Vane Pump, Transactions of the Japan Society of Mechanical Engineers Series B 58 (547) (1992) 799–803. `doi:10.1299/kikaib.58.799`.

[9] B. L. Jones, D. N. Johnston, D. K. Longmore, Simulation of Suction Flow Ripple in Power Steering Pumps, in: SAE Technical Paper, 1998, pp. 89–95. `doi:10.4271/982023`.

[10] M. Eaton, P. S. Keogh, K. A. Edge, The modelling, prediction, and experimental evaluation of gear pump meshing pressures with particular reference to aero-engine fuel pumps, Proceedings of the Institution of Mechanical Engineers, Part I: Journal of Systems and Control Engineering 220 (2006) 365–379. `doi:10.1243/09596518JSCE183`.

[11] M. Battarra, E. Mucchi, A method for variable pressure load estimation in spur and helical gear pumps, Mechanical Systems and Signal Processing 76-77 (2016) 265–282. `doi:10.1016/j.ymssp.2016.02.020`.

[12] X. Zhao, A. Vacca, Numerical analysis of theoretical flow in external gear machines, Mechanism and Machine Theory 108 (October 2016) (2017) 41–56. `doi:10.1016/j.mechmachtheory.2016.10.010`.

[13] M. Fabiani, S. Mancò, N. Nervegna, M. Rundo, G. Armenio, C. Pachetti, R. Trichilo, Modelling and Simulation of Gerotor Gearing in Lubricating Oil Pumps, in: SAE International Congress and Exposition, 1999. `doi:10.4271/1999-01-0626`.

[14] N. D. Manring, The Discharge Flow Ripple of an Axial-Piston Swash-Plate Type Hydrostatic Pump, Journal of Dynamic Systems, Measurement, and Control 122 (2) (2000) 263. doi:10.1115/1.482452.

[15] K. Hattori, H. Suzuki, J. Hasegawa, Design Method of Small-Ripple Vane Pump, in: SAE Technical Paper, 1987, pp. 83–90. doi:10.4271/871681.

[16] M. R. Cho, Vane tip detachment in a positive displacement vane pump, KSME International Journal 12 (5) (1998) 881–887. doi:10.1007/BF02945555.

[17] Y. Inaguma, K. Nakamura, Influence of leakage flow variation on delivery pressure ripple in a vane pump, Proceedings of the Institution of Mechanical Engineers, Part C: Journal of Mechanical Engineering Science 228 (2) (2014) 342–357. doi:10.1177/0954406213484669.

[18] R. Gellrich, A. Kunz, G. Beckmann, E. Broszeit, Theoretical and practical aspects of the wear of vane pumps Part A. Adaptation of a model for predictive wear calculation, Wear 181-183 (PART 2) (1995) 862–867. doi:10.1016/0043-1648(95)90208-2.

[19] A. Kunz, R. Gellrich, G. Beckmann, E. Broszeit, Theoretical and practical aspects of the wear of vane pumps Part B. Analysis of wear behaviour in the vickers vane pump test, Wear 181-183 (PART 2) (1995) 868–875. doi:10.1016/0043-1648(95)90209-0.

[20] E. Mucchi, A. Agazzi, G. D'Elia, G. Dalpiaz, On the wear and lubrication regime in variable displacement vane pumps, Wear 306 (1-2) (2013) 36–46. doi:10.1016/j.wear.2013.06.025.

[21] A. Giuffrida, R. Lanzafame, Cam shape and theoretical flow rate in balanced vane pumps, Mechanism and Machine Theory 40 (3) (2005) 353–369. doi:10.1016/j.mechmachtheory.2004.07.008.

[22] E. S. Taylor, Dimensional analysis for engineers, Oxford University Press, 1974.